APPLIED PHYSICS

Optical control of 4*f* orbital state in rare-earth metals

Nele Thielemann-Kühn[1]*, Tim Amrhein[1], Wibke Bronsch[1,2], Somnath Jana[3]†, Niko Pontius[3], Robin Y. Engel[4]‡, Piter S. Miedema[4], Dominik Legut[5,6,7], Karel Carva[6], Unai Atxitia[1,8], Benjamin E. van Kuiken[9], Martin Teichmann[9], Robert E. Carley[9], Laurent Mercadier[9], Alexander Yaroslavtsev[9,10]§, Giuseppe Mercurio[9], Loïc Le Guyader[9], Naman Agarwal[9]¶, Rafael Gort[9], Andres Scherz[9], Siarhei Dziarzhytski[4], Günter Brenner[4], Federico Pressacco[4], Ru-Pan Wang[4,11], Jan O. Schunck[4,11], Mangalika Sinha[4]#, Martin Beye[4]‡, Gheorghe S. Chiuzbäian[12], Peter M. Oppeneer[10], Martin Weinelt[1]**, Christian Schüßler-Langeheine[3]**

A change of orbital state alters the coupling between ions and their surroundings drastically. Orbital excitations are hence key to understand and control interaction of ions. Rare-earth elements with strong magneto-crystalline anisotropy (MCA) are important ingredients for magnetic devices. Thus, control of their localized 4*f* magnetic moments and anisotropy is one major challenge in ultrafast spin physics. With time-resolved x-ray absorption and resonant inelastic scattering experiments, we show for Tb metal that 4*f*-electronic excitations out of the ground-state multiplet occur after optical pumping. These excitations are driven by inelastic 5*d*-4*f*-electron scattering, altering the 4*f*-orbital state and consequently the MCA with important implications for magnetization dynamics in 4*f*-metals and more general for the excitation of localized electronic states in correlated materials.

INTRODUCTION

In ultrafast spin dynamics in metals, optically induced transitions in valence electronic states are the first excitation step. Recent experiments and theory identified direct consequences of these initial excitations for the spin dynamics: Optical intersite spin transfer between different atomic sites of transition metal (TM) compounds leads to enhanced speed and efficiency of demagnetization (*1*). Excitations of 4*f* electronic states in rare-earth (RE) metals have not been considered to contribute to magnetization dynamics so far. X-ray magnetic circular dichroism studies, searching for separate spin and orbital dynamics in TM-RE ferrimagnets (*2*, *3*) were implicitly looking for changes of the *f* electronic state, albeit without stating that. They ultimately remained without conclusions. In contrast to valence states in TMs, which can be easily optically excited, the dipole selection rules

make the cross section for optical 4*f* excitations in RE metals very small (*4*) in particular for pump-photon energies not resonant with 4*f*-4*f* transitions. Therefore, laser-driven 4*f*-spin dynamics must result from coupling to other degrees of freedom, such as to the lattice via phonons or to the directly laser excited 5*d*6*s* valence electrons. While nonparallel 4*f*-spin order can be efficiently quenched via angular momentum redistribution (*5*, *6*), the speed of demagnetization in 4*f* ferromagnets is closely connected to the 4*f*-spin-lattice coupling (*7–15*). Launching phonons in 4*f* metals requires energies of few milli–electron volts, which is enough to generate spin waves (*16*) and excitations within the 4*f* ground-state multiplet (*17*) but not enough to reach higher lying 4*f* electronic multiplet states: The lowest-lying *f*-*f* multiplet transitions that change the total angular momentum *J* usually require energies of hundreds of milli–electron volts (*18*).

The spin-polarized itinerant 5*d* electrons mediate the indirect exchange coupling between the 4*f* states of neighboring atoms (Ruderman-Kittel-Kasuya-Yosida interaction) and thus enable in equilibrium long-range order of the strongly localized 4*f* magnetic moments (*16*). Distinct 5*d* and 4*f* magnetic order dynamics observed in state-selective studies on different RE metals (*6*, *7*, *9*) indicate a more intricate interplay of 4*f* and 5*d* states in nonequilibrium, but details of the 5*d*-4*f* interaction after optical pumping have rarely been explored. Partly, this is the case because a combined theoretical description of *d* and *f* electronic structure is difficult (*19*); magnetic dynamics simulation based on models like Landau-Lifshitz-Gilbert equation (*7*, *20–22*) or the Microscopic Three Temperature Model (*14*, *23*, *24*) usually treat the 4*f* and 5*d* magnetic systems as a single spin system. We present here an analysis of the 5*d*-4*f* coupling mechanisms in nonequilibrium and show that this coupling induces changes in the 4*f* electronic state that are directly linked to spin and orbital dynamics: Orbital state transitions altering the total angular momentum *J* have immediate consequences for the 4*f*-spin lattice coupling, which should be reflected in spin dynamics.

With new pulsed x-ray sources and instrumentation at the European X-ray Free Electron Laser (EuXFEL) and the Free Electron Laser in Hamburg (FLASH), experimental approaches have recently become

[1]Freie Universität Berlin, Fachbereich Physik, Arnimallee 14, 14195 Berlin, Germany. [2]Elettra-Sincrotrone Trieste S.C.p.A., Strada statale 14 – km 163,5, 34149 Basovizza, Trieste, Italy. [3]Helmholtz-Zentrum Berlin für Materialien und Energie GmbH, Albert-Einstein-Str. 15, 12489 Berlin, Germany. [4]Deutsches Elektronen-Synchrotron DESY, Notkestraße 85, 22607 Hamburg, Germany. [5]VSB - Technical University Ostrava, IT4Innovations, 708 00 Ostrava, Czech Republic. [6]Charles University, Faculty of Mathematics and Physics, DCMP, 12116 Prague 2, Czech Republic. [7]Department of Condensed Matter Physics, Faculty of Mathematics and Physics, Charles University, CZ-121 16 Prague, Czech Republic. [8]Instituto de Ciencia de Materiales de Madrid, CSIC, Cantoblanco, 28049 Madrid, Spain. [9]European XFEL, Holzkoppel 4, 22869 Schenefeld, Germany. [10]Uppsala University, Department of Physics and Astronomy, P.O. Box 516, 75120 Uppsala, Sweden. [11]Universität Hamburg, Physics Department, Luruper Chaussee 149, 22761 Hamburg, Germany.[12]Sorbonne Université, CNRS, Laboratoire de Chimie Physique-Matière et Rayonnement, 75005 Paris, France.

*Corresponding author. Email: nele.thielemann-kuehn@fu-berlin.de

†Present address: Max Born Institute for Nonlinear Optics and Short Pulse Spectroscopy, 12489 Berlin, Germany.

‡Present address: Department of Physics, AlbaNova University Center, Stockholm University, S-10691 Stockholm, Sweden.

§Present address: MAX IV Laboratory, Lund University, P.O. Box 118, SE-221 00 Lund, Sweden.

¶Present address: Department of Physics and Astronomy (IFA), Aarhus University, Ny. Munkegade 120, 8000 Aarhus C, Denmark.

#Present address: Institute for X-ray Physics, University of Göttingen, 37077 Göttingen, Germany.

**These authors contributed equally to this work.

feasible that merge high energy and time resolution with core-state selective probing. For detecting the $4f$ electronic dynamics, we combined two complementary methods: x-ray absorption spectroscopy (XAS) and resonant inelastic x-ray scattering (RIXS), as schematically illustrated in Fig. 1A. The time-resolved XAS and RIXS experiments were performed at EuXFEL and FLASH, respectively (see Fig. 1, B and C, for experimental schemes). XAS (at the $3d$-$4f$ transition) probes the full $4f$ multiplet and hence the sum of all changes to the electronic structure (25). RIXS (at the $4d$-$4f$ transition) allows for a selective detection of a specific electronic excitation with high sensitivity (26). We combined these two techniques to track femtosecond changes in the $4f$ multiplet structure after exciting the $5d6s$ valence electrons in paramagnetic hcp Tb metal with near–infrared (IR)–laser pulses, and we observed distinct $4f$ orbital excitations. We show that variations of the $4f$ state are primarily driven by $5d$-$4f$ electron-electron scattering, but we also find indications of $5d$-$4f$ electron transfer in the $4f$ electron dynamics. The effect is not small: Under our experimental conditions, we observe $5d$-$4f$ electronic scattering to excite about 20% of the atoms in the probed volume. In addition, it is relevant: The altered spin and orbital angular momenta of the excited $4f$ electronic state affect the coupling of the $4f$ magnetic system to the environment. Density functional theory (DFT) calculations show that the observed orbital transitions can affect the magnetocrystalline anisotropy (MCA) such that the magnetic easy axis locally flips on a femtosecond timescale.

RESULTS
Time-resolved XAS and RIXS
As depicted by the experimental scheme in Fig. 1B, we recorded XAS spectra by probing the transmission through a thin Tb layer deposited on a silicon nitride membrane. We excited our sample with 800-nm-laser pulses (1.55 eV) and probed the XAS signal with monochromatized x-ray pulses from EuXFEL (see Materials and Methods). Time and energy resolution in the experiment was 65 fs and 350 meV, respectively. Figure 2A shows spectra recorded at the M_5 resonance, a transition into $3d^9 4f^9$ states, which leaves behind a $3d_{5/2}$ core hole. The blue dots reflect the Tb M_5 absorption spectrum with $4f$ electrons in the $4f^8 {}^7F_6$ ground state ("unpumped"). Recorded 150 fs after near-IR-laser excitation the orange dots ("pumped") show a spectrum with varied line shape, indicating that pumping has changed the $4f$ electronic state. A reference measurement on Gd under identical conditions [see the Supplementary Materials, fig. S1] shows no pump effect in the XAS signal. As we explain further below, this confirms that the effects seen for Tb XAS are, in fact, caused by changes of the $4f$ electronic structure.

In the RIXS setup shown in Fig. 1C, we excited a Tb metal layer epitaxially grown on a W(110) crystal with 1030-nm laser pulses (1.2 eV) and recorded the RIXS signal with monochromatic x-ray pulses from FLASH (see Materials and Methods). The time resolution was 300 fs, and we recorded spectra with an energy resolution of 140 meV. The RIXS spectra measured at the $N_{4,5}$ ($4d \rightarrow 4f$) transition (147.2 eV) are shown in Fig. 2B; the peaks in the spectra are
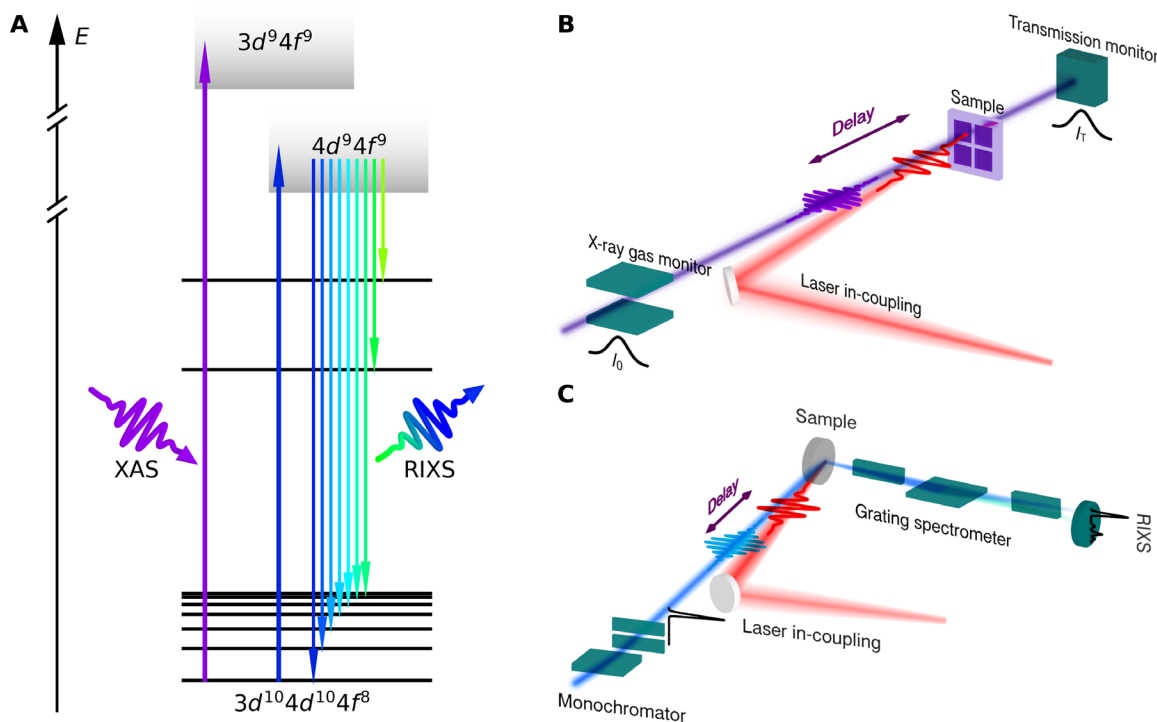

Fig. 1. XAS Tb M_5 and RIXS Tb $N_{4,5}$ experiment. (**A**) Scheme of the optical transitions in the x-ray absorption (XAS) and RIXS experiment. The black lines illustrate the energy levels in the $4f^8$ multiplet. (**B**) Sketch of the XAS experiment. Following the excitation with 1.55-eV photons, the transient absorption $log(I_T/I_0)$ is probed at the Tb M_5 edge in transmission geometry with 350-meV energy and 65-fs time resolution. The x-ray gas monitor is used to measure the incident intensity I_0. With the transmission intensity monitor, we determine the sample transmission I_T. (**C**) Sketch of the RIXS experiment. After exciting the sample with 1.2-eV-laser pulses, the RIXS signal is probed with x-ray pulses at the Tb $N_{4,5}$ resonance and with a time resolution of 300 fs. With the TRIXS grating spectrometer, we achieve an energy resolution of 140 meV.
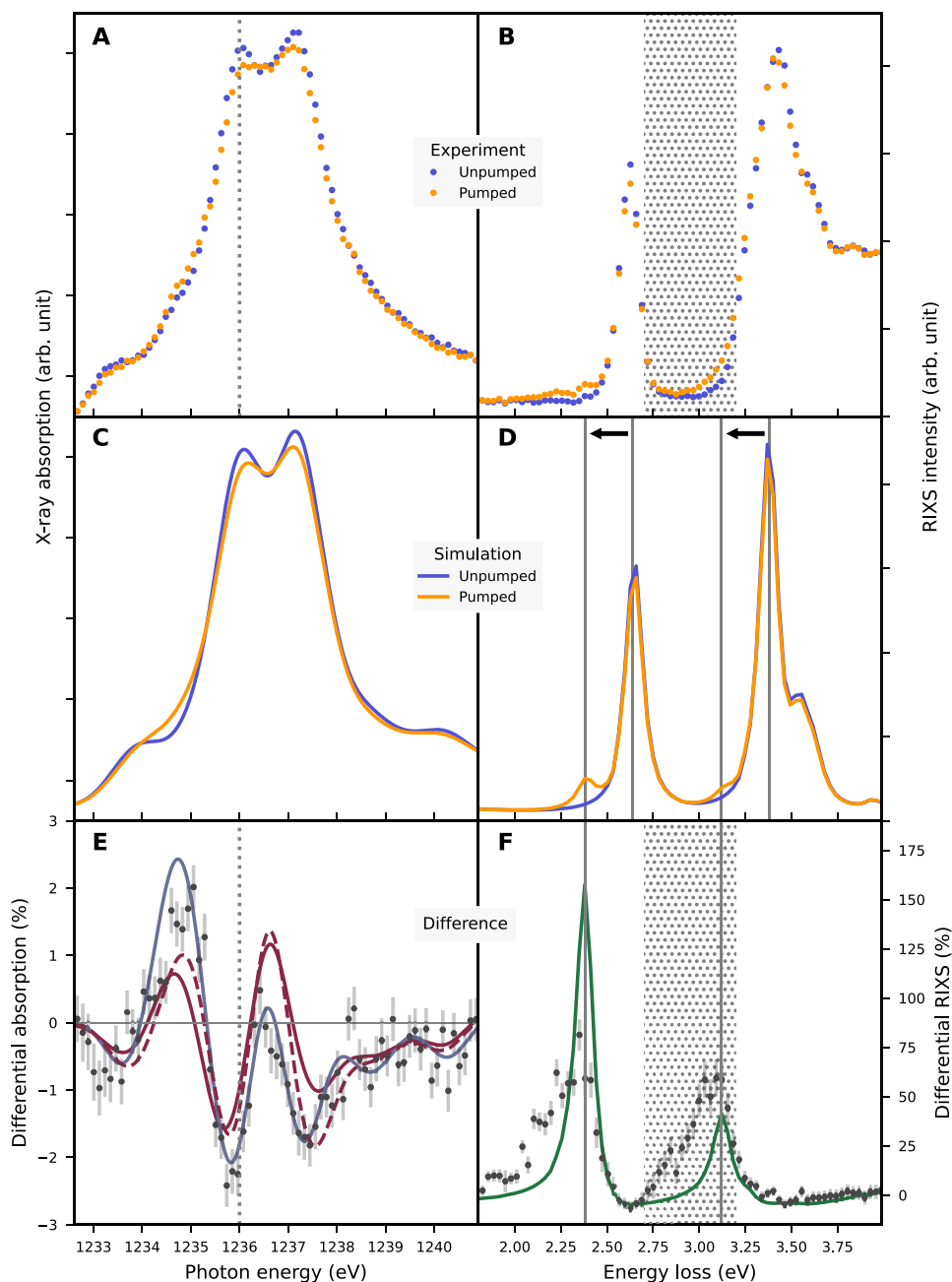
Fig. 2. Pump-induced changes in the XAS Tb M_5 and RIXS Tb $N_{4,5}$ spectra. (**A**) XAS spectrum of the Tb M_5 edge 150 fs after optical excitation (orange) in comparison to the spectrum for the unpumped sample (blue). The vertical line indicates the energy at which we recorded the pump-probe-delay trace (Fig. 3). (**B**) $N_{4,5}$ edge RIXS signal measured with 147.2-eV pulses for the unpumped Tb sample (blue) and 300 fs after pump-pulse excitation (orange). The hatched area marks the energy-loss window, over which we integrated the data to study the pump-probe-delay dependence (Fig. 3). (**C**) Simulation of the Tb M_5 spectra based on atomistic calculations. The blue line shows the pure Tb $4f^8\,^7F_6$ ground-state spectrum. The orange line shows the ground-state spectrum, including admixtures of the excited states $4f^7\,^8S_{7/2}$, $4f^8\,^7F_5$ and $4f^9\,^6H_{15/2}$. (**D**) Atomistic RIXS calculations for the pure $4f^8\,^7F_6$ ground state (blue line) and with admixture of the $4f^8\,^7F_5$ states (orange line). Horizontal arrows depict the shift of the main features by 0.26 eV ($^7F_6 \rightarrow {}^7F_5$). (**E**) Differential x-ray absorption, i.e., the relative change of the XAS signal between pumped and unpumped sample (black dots). Solid lines are fits based on atomistic calculations of the $^7F_6$ ground state with admixtures of $4f^8\,^7F_5$ (purple) and $4f^7\,^8S_{7/2}$, $4f^8\,^7F_5$, $4f^9\,^6H_{15/2}$ (blue). The dashed purple line is a fit assuming thermal occupation of the $4f^8$ multiplets. The vertical line indicates the energy at which we recorded the pump-probe-delay dependence. (**F**) Differential RIXS, i.e., the relative change of the RIXS signal between pumped and unpumped sample (black dots). The green line depicts the relative change between the calculated spectra in (D). Pump-probe delay–dependent data in Fig. 3 stem from integration over the energy-loss window marked by the hatched area.

related to electronic transitions into different final states in the $4f$ shell (Fig. 1A). The orange dots represent the spectrum 300 fs after excitation with the pump-laser pulse (pumped), which differs from that of the sample in the $4f^8\,{}^7F_6$ ground state (blue dots, unpumped). Both spectra are plotted over energy loss, i.e., the energy difference between incoming and scattered photons. The spectrum of the pumped sample shows a transfer of intensity from the main features at 2.7 and 3.4 eV to losses of around 2.4 and 3.1 eV, respectively, again indicating an excited $4f$ initial state.

To identify the particular excitations in the $4f$ multiplet, we describe the $4f$ ground- and excited-state XAS and RIXS spectra with atomic multiplet calculations (*27*, *28*) (see Supplementary Materials for details). On the basis of these calculated spectra, we simulate the spectra for the pumped and unpumped sample (see Fig. 2, C and D), as well as the differential change (relative change compared to the ground-state spectrum in %) in XAS and RIXS, respectively (see Fig. 2, E and F).

4f-5d inelastic scattering

We start with analyzing the RIXS spectra presented in Fig. 2B. The main pump-induced change is a shift of the two ground-state RIXS features at around 2.64 and 3.4 eV by about 0.26 eV to lower energies (black horizontal arrows in Fig. 2D). The observed energy difference matches the lowest-lying multiplet excitation that involves a change of J in the Tb $4f^8$ multiplets (${}^7F_6 \rightarrow {}^7F_5$, $\Delta J = -1$). We verify this interpretation by the simulation shown in Fig. 2 (D and F). We can reproduce the pump-induced spectral changes by including an admixture of $4f$ excited states to the description of the ground-state spectrum. As depicted by the orange line in Fig. 2D and the green line in Fig. 2F, adding a contribution of about 5% ${}^7F_5$ to the ${}^7F_6$ ground-state spectrum (blue line in Fig. 2D) yields already a reasonably good description of the transient changes in the RIXS data.

The RIXS cross section for specific $4f$ multiplets across the Tb $N_{4,5}$ resonance strongly depends on the incoming photon energy; their spectral weight is therefore not a good measure of the admixture of excited states in the probed volume. We better quantify the overall contribution of ${}^7F_5$ excitations from the XAS spectra measured at 150-fs pump-probe delay (Fig. 2A). The purple solid line in Fig. 2E with an admixture of about (16 ± 1) % ${}^7F_5$ qualitatively describes the overall shape of the differential absorption, thus giving a measure of the total contribution of ${}^7F_5$ excited states at 150-fs delay.

How is this excitation possible? As argued above, $4f$-$4f$ transitions directly induced by the pump pulse are negligible. For optical d-f excitations from the itinerant $5d$ valence states into the localized $4f$ states or vice versa, our pump-laser-photon energies are too low: These excitations require energies of 2.8 and 2.3 eV, respectively (*29*), while we pump with 1.55-eV photons for XAS and 1.2-eV photons for RIXS (two-photon absorption processes are negligible under our experimental conditions; see Supplementary Materials). The pump-laser excitation hence cannot alter the $4f$ state directly, but it heats the valence electrons of mixed $5d$ and $6s$ character, which then can transfer the excitation to the $4f$ system.

The idea that such a $5d6s$-$4f$ energy transfer is the relevant process here, is revealed by the temporal evolution of XAS and RIXS spectral changes. In Fig. 3, we present the differential absorption measured at 1236 eV (marked by the vertical line in Fig. 2, A and E) versus the delay between the IR-pump and x-ray-probe pulse (black data points). The absorption at this energy drops rapidly with a decay constant of 70 fs, reaches a maximum deviation from the
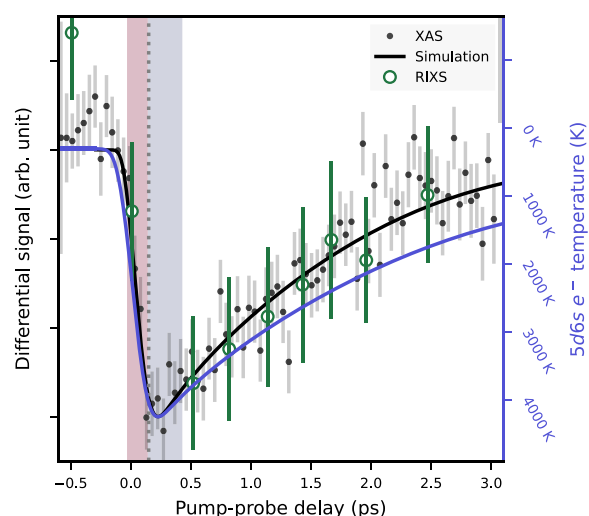

Fig. 3. Pump-probe delay–dependent changes in XAS Tb M_5 and RIXS Tb $N_{4,5}$ spectra. Differential XAS (black dots) and RIXS signal (green markers) as a function of pump-probe delay. The XAS signal was measured at a photon energy of 1236 eV (vertical lines in Fig. 2, A and E). The RIXS signal is integrated over the energy loss region 2.7 to 3.2 eV as marked in Fig. 2 (B and F). For comparison with XAS data, the y-scale is inverted. The $5d6s$ electron temperature T_{el} (blue solid line) has been calculated by the two-temperature model (see Supplementary Materials). The black solid line depicts the temperature evolution of those electrons that can actually induce the $4f$ excitation observed in XAS. The colored bars indicate the time intervals over which we integrated the differential absorption shown in Fig. 5 (B and C).

ground state of 3% after 200 fs, and recovers with a time constant of about 3 ps (see Supplementary Materials, fig. S2). The transient change in the energy-loss region 2.7 to 3.2 eV of the RIXS spectra (hatched area in Fig. 2, B and F) recorded with a lower time resolution of 300 fs follows the same trend (see Fig. 3, green markers). These observed timescales resemble those for optically excited valence electrons in metals (*30*, *31*): The blue line in Fig. 3 shows the temperature of the $5d6s$ electronic system calculated with a two-temperature model (2TM), involving $5d6s$ electrons and phonons (see Supplementary Materials). The electron-temperature curve qualitatively matches the transient differential change in the XAS and RIXS signal at 1236 eV. We infer that the $4f$ multiplet is only excited in the presence of hot $5d6s$ electrons. We assign the mechanism for the ${}^7F_6 \rightarrow {}^7F_5$ excitations in the $4f$ shell to inelastic $5d$-$4f$ electronic scattering, involving transfer of energy and angular momentum from the optically excited $5d6s$ electrons to the $4f$ system. As only $5d6s$ electrons with enough energy can induce the $4f$ transition, we better compare the differential spectral changes with the transient population of those hot electrons, that actually can transfer the energy required for the ${}^7F_6 \rightarrow {}^7F_5$ transition by filling a $5d$ holes at respectively lower energies (black line in Fig. 3; see Supplementary Materials for details). This curve yields an even better fit to the XAS and RIXS data, supporting our assumption about the underlying scattering process.

In Fig. 4, we illustrate the supposed mechanism in a total-energy scheme for the relevant channels in XAS and RIXS, explaining the spectroscopic signatures of the $4f$-multiplet excitation. In XAS at the M_5 resonance $3d$ electrons are excited from the initial state $3d^{10}4d^{10}4f^8(5d6s)^3$ to the $3d^94f^9$ final states (purple arrows). In RIXS at the N_4 edge, $4d$ electrons are excited from the initial state
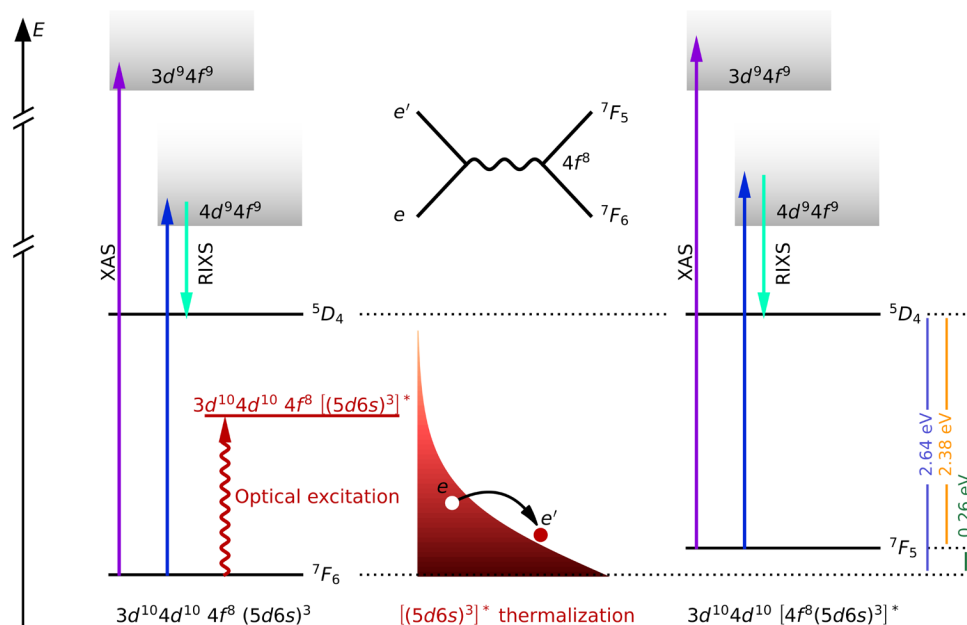
Fig. 4. Total-energy scheme of the transitions involved in the XAS and RIXS experiment. Left: $3d$ ($4d$) electrons are excited at the M_5 (N_4) resonance in XAS (RIXS), provoking a transition from the initial state $3d^{10}4d^{10}4f^8(5d6s)^3$ to $3d^94f^9$ final ($4d^94f^9$ intermediate) states [purple (blue) arrows]. In the initial state, the $4f^8$ electrons occupy the $^7F_6$ ground-state multiplet. The intermediate state in RIXS decays to a final state involving the $^5D_4$ multiplet (energy loss = 2.64 eV; compare RIXS spectra in Fig. 2B). Optical excitation by the pump laser elevates the full electron system from the ground state (red arrow) by exciting the $(5d6s)^3$ electrons. Middle: The hot $[(5d6s)^3]^*$ electrons rapidly thermalize to a Fermi distribution (red area). Via inelastic electronic $5d$-$4f$ scattering (Feynman diagram) energy and angular momentum is transferred between the $(5d6s)^3$ and $4f^8$ electronic system. This leads to a $^7F_6 \rightarrow {}^7F_5$ transition (0.26 eV) with the $5d$ electron filling a hole of lower energy (−0.26 eV). Right: When the initial state for RIXS has changed to the higher lying $^7F_5$ multiplet, the RIXS feature associated with the decay to $^5D_4$ shifts by 0.26 eV to smaller energy losses. The XAS spectral shape changes compared to that from the $^7F_6$ state (Fig. 2C and fig. S4 in the Supplementary Materials).

$3d^{10}4d^{10}4f^8(5d6s)^3$ to the $4d^94f^9$ intermediate states (blue arrows). In the Tb ground state, the $4f^8$ electrons occupy the $^7F_6$ multiplet. Optical excitation by the pump laser elevates the complete ground state (red arrow) by exciting the $(5d6s)^3$ electrons. They rapidly thermalize by screened Coulomb interaction and become Fermi distributed (indicated by the red area in the middle section of Fig. 4). By inelastic electronic $5d$-$4f$ scattering (Feynman diagram in the top middle section), energy and angular momentum are transferred between the $(5d6s)^3$ and $4f^8$ electronic system. A $4f$ electron is excited from $^7F_6$ to $^7F_5$, and a $5d$ electron fills a hole of lower energy. On sites where this happens, the initial state in XAS and RIXS changes (right side of Fig. 4). In XAS, this affects the spectral line shape (compare Fig. 2A). In RIXS, the raise of the initial state energy causes a red shift of the energy loss features (compare Fig. 2, B and D, with the energy loss values given in the right section of Fig. 4). The $^7F_6 \rightarrow {}^7F_5$ transition implies a change of angular momentum $\Delta J = -1$. A spin flip, and altering the $5d$ spin by $\Delta S = 1$ would conserve the total angular momentum in the scattering process.

How about the excitations of energetically higher lying multiplets ^7F_J with $J = 4,3,2,1,0$? Such transitions require an angular momentum transfer $\Delta J < -1$. Either multiple $5d$-$4f$ electronic scattering events each involving $\Delta S = 1$ or a transfer of angular momentum from the reservoir of quenched $5d$ orbital momenta might permit higher ΔJ changes. Including the contribution of higher $4f^8$ multiplets to the pumped XAS spectrum (assuming a thermal occupation, weighted with a Boltzmann factor and degeneracy $2J + 1$; see Supplementary Materials for details) improves the fit to the differential XAS (dashed purple line in Fig. 2E). Also, the asymmetric

peak profile in the differential RIXS (black markers in Fig. 2F) could come from energetically higher lying excitations within the $4f$ states. Yet, with the presently available experimental data, we cannot answer the question unequivocally: The slightly better fit to the XAS data does not really prove these transitions, and the discontinues variation of energy resolution along the energy axis in the RIXS spectra makes the detection of the corresponding RIXS features difficult. We further found no evidence for these higher $4f^8$ states from features on the anti-Stokes side of the spectra (see Supplementary Materials for details). However, we find indications for other $4f$ excitations as we discuss in the following.

5d-4f electron transfer

We notice that the shape of the pumped XAS spectrum is not constant but changes with pump-probe delay. Figure 5A presents an energy vs. delay map illustrating the differential absorption up to 430 fs after pumping. Difference spectra (dots in Fig. 5, B and C) averaged over two successive delay ranges I and II (marked in Fig. 5A by black vertical lines and color-coded in Fig. 3) show that the dip at 1235.8 eV becomes more pronounced at larger pump-probe delays while the one at 1237.5 eV changes only slightly: Obviously, the $4f$ state evolves in time. The simulated differential XAS changes from excitation of higher ^7F_J multiplets ($J = 4,3,2,1,0$) do not explain the evolution of the pronounced pump effect at 1235.8 eV (see Supplementary Materials for spectral contribution of different ^7F_J multiplets). Therefore, we discuss the possibility of excitation into $4f^9$ and $4f^7$ multiplets.
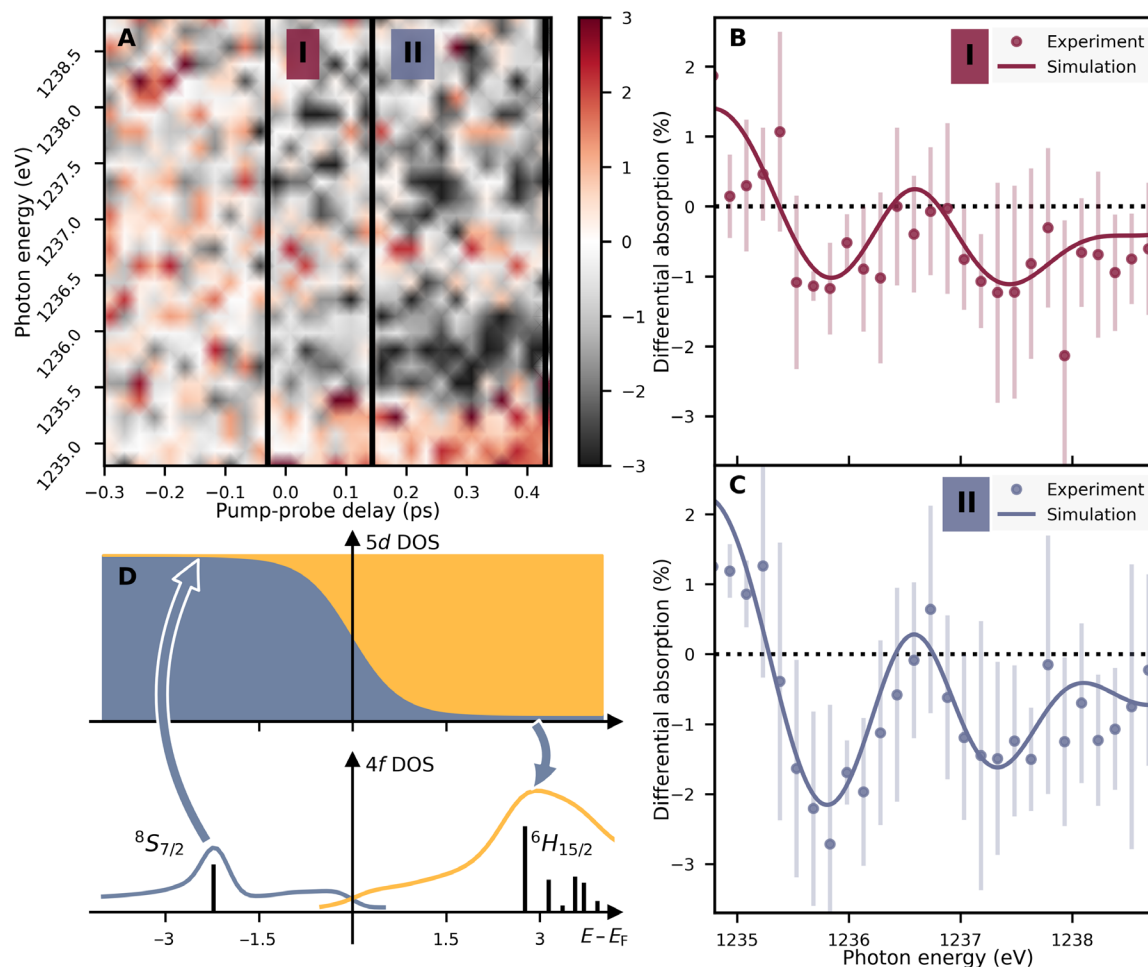
Fig. 5. Pump-probe delay–dependent variations in the Tb M_5 excitation multiplet. (**A**) Map of differential x-ray absorption over photon energy (Tb M_5 edge) and pump-probe delay. We integrated the data in the time intervals I and II (black vertical lines, color-coded in Fig. 3) and obtained the results shown in (B) and (C). (**B**) From the map in (A), deduced energy-dependent differential absorption (dots) integrated over interval I (−0.03 ps to 0.143 ps). The solid line is a simulation including $4f^7$ and $4f^9$ electron-transfer contributions [$4f^7\,^8S_{7/2}$ (2 ± 0.2%), $4f^8\,^7F_5$ (11.3 ± 0.8%), and $4f^9\,^6H_{15/2}$ (1.2 ± 0.5%)]. (**C**) From the map in (A), deduced energy-dependent differential absorption (dots) integrated over interval II (0.143 to 0.43 ps). The solid line represents a simulation including increased $4f^7$ and $4f^9$ contributions compared to the simulation shown in (B) [$4f^7\,^8S_{7/2}$ (2.8 ± 0.2%), $4f^8\,^7F_5$ (19.7 ± 0.8%), and $4f^9\,^6H_{15/2}$ (4.8 ± 0.4%)]. (**D**) Within 100 fs after optical excitation, $5d$ valence electrons form a hot Fermi distribution (dark gray area). Besides $^7F_5$ contributions from inelastic $5d$-$4f$ scattering, $5d$-$4f$ electron transfer possibly leads to $4f^7$ and $4f^9$ final states. The lower panel shows the $^8S_{7/2}$ final state of photoemission at 2.3 eV below E_F and the $^6H_{15/2}$ final state of inverse photoemission at 2.8 eV above E_F (29). DOS, density of states.

The pump-excitation energy in our experiment is not sufficient to directly excite states with varied $4f$ electron number: The transitions to a $4f^9$ ($^6H_{15/2}$) or $4f^7$ ($^8S_{7/2}$) multiplet requires 2.8 and 2.3 eV, respectively (29). However, once thermalized, the Fermi distribution of the hot valence electrons extends beyond the initial pump energy; electrons at 2.8 eV above the Fermi energy can fill an empty $4f$ state, and holes 2.3 eV below E_F can accept the most lightly bound minority spin electron of Tb via elastic tunneling processes (see illustration in Fig. 5D).

By including $4f^9$ and $4f^7$ multiplets in our XAS simulation, we can achieve a quantitative description of the reported spectral changes at 150-fs delay in Fig. 2A. The best fit (blue solid line in Fig. 2E) contains (20 ± 1) % of the $^7F_5$ excited $4f^8$ states and (4.5 ± 0.7) % of $4f^9$ and (3.3 ± 0.2) % of $4f^7$ electron-transfer contributions. We find our assumption of $4f^7$ and $4f^9$ contributions supported by the spectral changes on short delay scales presented in Fig. 5. As these states become populated only after the $5d6s$-electron system has thermalized,

we expect lower contributions before the maximum electron temperature is reached. We can describe the spectral changes with delay in Fig. 5 (B and C) by different $4f^7$ and $4f^9$ contributions (solid lines). The $4f^9$ weight grows from (1.2 ± 0.5) % in interval I to (4.8 ± 0.4) % in interval II, for $4f^7$ it grows from (2 ± 0.2) % to (2.8 ± 0.2) %.

Including $4f^7$ and $4f^9$ multiplets in the simulation requires some assumptions. The spectral shape itself can readily be simulated (and experimentally observed in Gd and Dy, respectively). Unlike for the orbital-excited $4f^8$ states, though, our atomic multiplet calculation does not provide the energy position of the $4f^7$ and $4f^9$ multiplets relative to $4f^8$. The relative energy depends critically on core-hole screening, which is altered by adding or removing a localized $4f$ electron. We determined the effect on the core-hole screening by optimizing the energy shift to match the experimental data (see Supplementary Materials for details).

There are issues with the $5d$-$4f$ electron transfer interpretation that we discuss in the following: First, only about 0.1% of the $5d$

electrons/holes at 4000 K (peak temperature from the 2TM calculations) will exhibit energies compatible with respective tunneling processes. To cause the observed effects, this channel must be very efficient. This at least is possible as the coupling between $5d$ and $4f$ states is rather strong (32). Second, we observe no indications of $4f$-$5d$ transitions in the RIXS data. As stated above, however, the RIXS cross section for specific $4f$ multiplets strongly varies with x-ray energy. We may have just missed these excitations with the particular photon energy of 147.2 eV. Last, the contribution of the $4f^9$ seems to increase more than that of the $4f^7$ when going to longer delays. We speculate that this may be related to the different $5d$ density of states below and above E_F, affecting the $5d$-$4f$ overlap. We note here again that there is no common way to describe both the $4f$ and $5d$ electronic structure of RE metals in the same model and that a quantitative calculation of d-f scattering and electron transfer is currently beyond the state-of-the-art.

For Gd, which we used for a reference XAS measurement (see Supplementary Materials, fig. S1), all the excitations discussed for Tb would occur at much higher energies; the lowest possible excitation out of the $^8S_{7/2}$ $4f$ multiplet requires an energy of 4.1 eV (29). The fact that we observe no spectral change in Gd XAS shows that all changes seen in Tb XAS are related to $4f$ electronic changes and not caused by other pump effects.

DISCUSSION
Transient angular momentum change
While open questions remain for the excitations of higher $4f^8$ multiplets and the $5d$-$4f$ electron transfer, the XAS and RIXS data show the $4f^8$ $^7F_6 \rightarrow {}^7F_5$ multiplet excitation without any doubt as the dominant effect. This helps understanding angular momentum transfer in nonequilibrium magnetization dynamics of Tb and other RE ions. Excitations of $4f$ state need to be included in a full description of nonequilibrium processes, particularly because they could affect the coupling between the $4f$ system and the lattice, an important channel in magnetic dynamics of RE metals (3, 7).

The effect of $4f$ orbital excitation goes beyond a mere rescaling of the $4f$-phonon coupling. We validate this effect by investigating the influence of the $4f^8$ $^7F_5$ excited states on the MCA. At room temperature in the paramagnetic phase of Tb, all m_J levels ($J = -6 \ldots +6$) of the $^7F_6$ multiplet are occupied (17). In the ferromagnetic phase at low temperatures, the m_J level splitting increases and the energetically lowest configuration $m_J = 6$ ($m_\ell = 3$, $m_s = 3$) becomes preferentially occupied. To estimate the MCA change, we compare a Tb $m_\ell = 3$ ground state with an $m_\ell = 2$ state, which (together with spin-flip $m_s = 2$ states) forms the lowest $m_J = 5$ level of the $4f^8$ $^7F_5$ multiplet: $|m_J = 5> = 1/\sqrt{2} \, |m_\ell = 2, m_s = 3> + 1/\sqrt{2} \, |m_\ell = 3, m_s = 2>$. From the $m_s = 2$ contributions, we expect a minor impact on the MCA but a considerable one from $m_\ell = 2$. We therefore determined the MCA for the Tb $m_\ell = 3$ ground state and the $m_\ell = 2$ excited state from all-electron first-principles calculations (see Materials and Methods). For the ground state, our ab initio calculations provide an MCA of 15 meV per atom with a preferential orientation of magnetic moments (easy axis) in the hcp basal plane along the crystallographic a axis, both of which are consistent with experiment (33). When we modify the minority Tb $4f$-electron occupation to the $m_\ell = 2$ state and perform a one-step calculation of the total energies, we find a rotation of the easy axis: magnetization

along the c axis perpendicular to the basal plane becomes favorable. We verified this result by creating a self-consistent state with dominant $m_\ell = 2$ occupation by modifying the Coulomb repulsion between the $4f$ electrons (adjustment of Hubbard U), which, likewise flips the easy axis.

While we could prove the $^7F_6 \rightarrow {}^7F_5$ transition, the data indicate additional $4f$ excitations with minor weight and a time-dependent contribution of different excited states. In addition to the changes of the MCA, also contributions to ultrafast demagnetization could matter, e.g., by thermal occupation of the $4f$ states or via electron-transfer transitions. The latter could principally quench the MCA by orders of magnitude by creating Gd-like configurations (7).

Our work stands apart from studies on $4f$ orthoferrites, where the RE ions (R) are placed in noncentrosymmetric positions of the $RFeO_3$ crystal lattice (34–38). As a consequence of symmetry breaking, resonantly driven electric dipole transitions dominate the observed dynamics. A resulting change of MCA provokes reorientation of the Fe spins in the crystal lattice; a transition which is also induced by thermal heating (39). We report on an ultrafast change of $4f$ orbital states, based on inelastic electron-electron scattering between itinerant $5d$ and localized $4f$ electrons.

Perspectives
In the Tb XAS experiment we altered the $4f$ state of about 20% of all atoms (compare best fit, blue solid lines in Fig. 2E), which is quite sizeable. With a simple estimate, we find a transfer of roughly 10% of the absorbed laser energy into the $4f$ system (see Supplementary Materials). The excitation density might be further enhanced and specific transitions selectively driven by resonant pump-laser excitation. Shaping of the valence band structure by combining, e.g., $3d$ and $4f$ metals in alloys or multilayers could also affect the efficiency and selectivity of the $4f$ electronic excitations.

Our findings are particularly relevant in view of recent reports on all-optical switching (AOS) in Tb-based compounds (40–42). Compared to AOS materials comprising magnetically soft Gd, the strong MCA in Tb promises stable domains on the nanometer scale. The dynamics, however, appear to be more intricate in Tb-based systems; the accepted model describing AOS in Gd-based compounds fails. Our conclusion about the suppressed $4f$ excitations in Gd and their dominant contribution in Tb gives another context to the discussion on AOS in Tb-based compounds.

Our findings identify a fundamental excitation mechanism, based on $5d$-$4f$ inelastic electronic scattering. This so far disregarded process is highly relevant for optically induced magnetization dynamics in $4f$ metals and their compounds, as it provides basic insights to atomic spin and orbital dynamics, as well as to nonequilibrium $5d$-$4f$ coupling mechanisms. The presented electronic scattering channel might be exploited to optically control material parameters in magnetically ordered metals and further correlated materials. The ultrafast handle to transiently manipulate MCA may be functionalized for, e.g., writing bits in high density magnetic storage devices.

MATERIALS AND METHODS
X-ray absorption at the SCS station of EuXFEL
We performed the x-ray absorption experiment at the EuXFEL SCS Instrument (43), making use of the high energy resolution ($E/\Delta E \approx 3500$) in the energy range around the Tb and Gd $3d$ to $4f$

($M_{5,4}$) resonances. We recorded high-resolution x-ray absorption spectra using the x-ray gas monitor for measurement of the incident intensity I_0 and the transmission intensity monitor—a cwd diamond scintillator—to determine the sample transmission I_T. The XAS signals (Fig. 2A) are calculated via $-log(I_T/I_0)$. The time-resolved XAS measurements were performed with 350-meV energy resolution. The 65-fs time resolution was determined by cross-correlation of optical pump and x-ray probe pulses. For longer intervals of data recording, the time resolution was 100 to 200 fs (data shown in Fig. 5). For exciting the samples, we used 800-nm pulses ($h\nu = 1.55$ eV) from the SASE3 PP laser system. The incident pump fluence was (10 ± 2) mJ/cm^2. The laser-spot size was (0.28×0.2) mm^2 and thus larger than the x-ray-probe beam of (0.1×0.1) mm^2, ensuring a nearly homogeneous excitation profile in the x-ray spot.

RIXS at the PG1 beamline of FLASH I
We conducted the RIXS experiments at the PG1–TRIXS permanent end station (44) (RIXS spectrometer for Time-resolved Resonant X-Ray Scattering) located at FLASH. The PG1 beamline can reach energies from 36 to 250 eV with high intensity and an energy resolution of about 0.07%, ideal for investigating RIXS at the $N_{4,5}$ resonance of Tb around 147 eV. The experiment was performed at a grazing incident angle of about 25°, and photons were collected under 105° with respect to the sample surface. The outgoing photons are dispersed according to their energy by a grating spectrometer and recorded on an x-ray charge-coupled device camera. In focus, the RIXS grating spectrometer provides a resolution of about 100 meV/px at 147 eV, corresponding to about 140-meV total resolution in the spectrum. Off-focus, the resolving power decreases according to the dispersion and because of the refocusing off-axial parabolic mirror. This results in a variation of the energy resolution across the probed energy-loss region. For the RIXS data shown in Fig. 2 (B and F), the spectrometer focus was optimized at 2.5-eV energy loss. For pumping, we used near-IR-laser pulses of 1030-nm wavelength ($h\nu = 1.2$ eV) and achieved a time resolution of 300 fs (45). The incident pump fluence was 20 mJ/cm^2. The laser-spot size was (150×150) μm^2, and the x-ray probe beam on the sample was (20×40) μm^2, ensuring a nearly homogeneous pump profile within the probed area. To record time traces (Fig. 3), we used a delay hopping routine randomly switching between delays to exclude unknown cross-correlations.

Statistical analysis
For the XAS and RIXS signals from the pumped and unpumped samples, we take the SE for absorption and scattered signal, respectively. For the differential change of the signals (Figs. 2, E and F, and 3), we deduce uncertainties from error propagation. The uncertainties for the differential change of absorption in the time intervals I and II of the energy-delay map (Fig. 5, B and C) stem from the SD in each energy-delay bin.

Samples
In the XAS experiment, we studied polycrystalline Tb and Gd transmission samples of 10-nm thickness. To prevent oxidation, the RE metal was sandwiched between yttrium layers. The samples were grown on an aluminum heat sink on a silicon nitride membrane, resulting in the following structure Y(2)/RE(10)/Y(25)/Al(300)/SiN(100), where RE = Tb and Gd. Numbers in brackets give the layer thickness in nanometers. The Tb and Gd samples were measured at room temperature in the paramagnetic phase.

For the RIXS study, we grew a thicker Tb film (40 nm) to maximize the number of absorbed photons and therewith the count rate in the RIXS signal. The film was grown by molecular beam epitaxy (MBE) on a W(110) single crystal, prepared and characterized by x-ray magnetic circular dichroism at the PM3 beamline of BESSY II (Helmholtz-Zentrum Berlin) (46). To prevent the Tb film from oxidation, the sample was capped with a sputtered 4-nm layer of Ta resulting in the following sample composition: Ta(4 nm)/Tb(40 nm)/W(110). The RIXS measurements were performed in the paramagnetic phase of Tb at room temperature.

Atomic multiplet calculations of $M_{4,5}$ edge XAS and $N_{4,5}$ edge RIXS
Because of the localized character of the 4f states, the shape of the absorption multiplets can be simulated even for laser-excited samples (27). The atomic multiplet calculations are performed using the Quanty simulation package (47–49). Details on the quantum chemical treatment of the atomic multiplet calculations of the x-ray spectra can be found in sections S4 to S6 of the Supplementary Text as well as in the book by de Groot and Kotani (27, 50). We do not simulate 4f-5d interaction; we calculate atomistic XAS and RIXS spectra for different 4f configuration and occupation, which are superposed to describe the spectral changes.

For our approach in treating the x-ray absorption cross section, it is assumed that for 4f RE compounds, the 4f-4f as well as the 3d-4f-two-particle interactions are most important for the description of the $M_{4,5}$ (3d) x-ray absorption spectrum. Because of the large wave-function overlap, the dipole term is dominated by $4f^n$ to 3d $^9 4f^{n+1}$ transitions. The calculations are based on spherical wave functions; a good approximation as spin-orbit interaction dominates crystal-field (CF) effects in RE 4f metals. The interactions between the 3d core and 4f states in these atomic multiplet calculations are explicitly taken into account via the so-called Slater-Condon parameters. The Slater-Condon parameters used in this work were taken from Thole's multiplet extension (51) to the Cowan code (52), which underlies the CTM4XAS interface maintained by de Groot (50). The complete set of values can be found in tables S1 to S3. To correct for the Hartree-Fock overestimation of electron-electron interaction, the Slater reduction factors were set to $F_{ff} = 0.61$, $G_{df} = 0.70$, and $F_{df} = 0.80$ for the $M_{4,5}$ edge XAS calculations.

For the simulation of RIXS at the $N_{4,5}$ edge, the Kramers-Heisenberg formula was applied. The scattering geometry was set to 105° emission and 25° incident angles according to the experimental setup. The reduction factors were set to $F_{ff}^2 = 0.80$, $F_{ff}^4 = 0.91$ and $F_{ff}^6 = 0.91$, $G_{df} = 0.60$ and $F_{df} = 0.60$ for the $N_{4,5}$ edge calculations.

DFT calculations
We performed DFT calculations, using the full-potential linear augmented plane wave method in the local spin-density approximation (LSDA), as implemented in the programs ELK (53) and WIEN2k (54). Spin-orbit coupling is crucial in 4f systems, where it is stronger than the CF, and has been included in the calculations. The full Brillouin zone has been sampled by about 2000 k-points. Strong electron-electron correlations present in the Tb 4f states were included in terms of the Hubbard correction U and Hund's parameter J (55). The DFT + U double counting was treated in the fully localized limit. For $U = 9$ eV and $J = 0.5$ eV, we obtain the self-consistent

ground-state Tb configuration with $m_\ell = 3$ and 15-meV MCA. The Tb configuration with $m_\ell = 2$ is self-consistently obtained for $U = 4$ eV and $J = 0.5$ eV. In the calculations where the $m_\ell = 2$ configuration was enforced without changing U, we used the magnetic force theorem to obtain the MCA through a one-step total energy calculation. For the MCA calculations, an increased accuracy of the muffin-tin potential and charge density expansion into spherical harmonics was used, with $\ell_{max} = 14$. MCA calculations for $4f$-based systems are often performed by mapping the full Hamiltonian to a CF Hamiltonian, where DFT calculations essentially provide the relevant CF parameters. The inaccuracies introduced by this mapping have been compared previously to LSDA-based calculations (56, 57) or DFT + U calculations similar to ours (58). These approaches involve different approximations; for example, the CF mapping assumes that the CF is independent of the orientation of the $4f$ shell. On the other hand, the DFT + U calculations are highly sensitive to the choice of U.

Supplementary Materials

This PDF file includes:

Supplementary Text
Figs. S1 to S11
Tables S1 to S6
Code S1
References

REFERENCES AND NOTES

1. F. Willems, C. von Korff Schmising, C. Strüber, D. Schick, D. Engel, J. K. Dewhurst, P. Elliott, S. Sharma, S. Eisebitt, Optical inter-site spin transfer probed by energy and spin-resolved transient absorption spectroscopy. *Nat. Commun.* **11**, 871 (2020).

2. N. Bergeard, V. López-Flores, V. Halté, M. Hehn, C. Stamm, N. Pontius, E. Beaurepaire, C. Boeglin, Ultrafast angular momentum transfer in multisublattice ferrimagnets. *Nat. Commun.* **5**, 3466 (2014).

3. M. Hennecke, I. Radu, R. Abrudan, T. Kachel, K. Holldack, R. Mitzner, A. Tsukamoto, S. Eisebitt, Angular momentum flow during ultrafast demagnetization of a ferrimagnet. *Phys. Rev. Lett.* **122**, 157202 (2019).

4. W. Demtröder, *Atoms, Molecules and Photons: An Introduction to Atomic-, Molecular- and Quantum Physics* (Springer Berlin, 2010).

5. N. Thielemann-Kühn, D. Schick, N. Pontius, C. Trabant, R. Mitzner, K. Holldack, H. Zabel, A. Föhlisch, C. Schüßler-Langeheine, Ultrafast and energy-efficient quenching of spin order: Antiferromagnetism beats ferromagnetism. *Phys. Rev. Lett.* **119**, 197202 (2017).

6. L. Rettig, C. Dornes, N. Thielemann-Kühn, N. Pontius, H. Zabel, D. L. Schlagel, T. A. Lograsso, M. Chollet, A. Robert, M. Sikorski, S. Song, J. M. Glownia, C. Schüßler-Langeheine, S. L. Johnson, U. Staub, Itinerant and localized magnetization dynamics in antiferromagnetic ho. *Phys. Rev. Lett.* **116**, 257202 (2016).

7. B. Frietsch, A. Donges, R. Carley, M. Teichmann, J. Bowlan, K. Döbrich, K. Carva, D. Legut, P. M. Oppeneer, U. Nowak, M. Weinelt, The role of ultrafast magnon generation in the magnetization dynamics of rare-earth metals. *Sci. Adv.* **6**, eabb1601 (2020).

8. B. Andres, M. Christ, C. Gahl, M. Wietstruk, M. Weinelt, J. Kirschner, Separating exchange splitting from spin mixing in gadolinium by femtosecond laser excitation. *Phys. Rev. Lett.* **115**, 207404 (2015).

9. B. Frietsch, J. Bowlan, R. Carley, M. Teichmann, S. Wienholdt, D. Hinzke, U. Nowak, K. Carva, P. M. Oppeneer, M. Weinelt, Disparate ultrafast dynamics of itinerant and localized magnetic moments in gadolinium metal. *Nat. Commun.* **6**, 8262 (2015).

10. M. Teichmann, B. Frietsch, K. Döbrich, R. Carley, M. Weinelt, Transient band structures in the ultrafast demagnetization of ferromagnetic gadolinium and terbium. *Phys. Rev. B* **91**, 014425 (2015).

11. R. Carley, K. Döbrich, B. Frietsch, C. Gahl, M. Teichmann, O. Schwarzkopf, P. Wernet, M. Weinelt, Femtosecond laser excitation drives ferromagnetic gadolinium out of magnetic equilibrium. *Phys. Rev. Lett.* **109**, 057401 (2012).

12. I. Radu, K. Vahaplar, C. Stamm, T. Kachel, N. Pontius, H. A. Dürr, T. A. Ostler, J. Barker, R. F. L. Evans, R. W. Chantrell, A. Tsukamoto, A. Itoh, A. Kirilyuk, T. Rasing, A. V. Kimel, Transient ferromagnetic-like state mediating ultrafast reversal of antiferromagnetically coupled spins. *Nature* **472**, 205–208 (2011).

13. M. Wietstruk, A. Melnikov, C. Stamm, T. Kachel, N. Pontius, M. Sultan, C. Gahl, M. Weinelt, H. A. Dürr, U. Bovensiepen, Hot-electron-driven enhancement of spin-lattice coupling in Gd and Tb 4f ferromagnets observed by femtosecond X-ray magnetic circular dichroism. *Phys. Rev. Lett.* **106**, 127401 (2011).

14. B. Koopmans, G. Malinowski, F. Dalla Longa, D. Steiauf, M. Fähnle, T. Roth, M. Cinchetti, M. Aeschlimann, Explaining the paradoxical diversity of ultrafast laser-induced demagnetization. *Nat. Mater.* **9**, 259–265 (2010).

15. A. Melnikov, A. Povolotskiy, U. Bovensiepen, Magnon-enhanced phonon damping at Gd(0001) and Tb(0001) surfaces using femtosecond time-resolved optical second-harmonic generation. *Phys. Rev. Lett.* **100**, 247401 (2008).

16. J. Jensen, A. R. Mackintosh, *Rare Earth Magnetism* (Clarendon Press, 1991).

17. K. Lin, G. Li, S. Khmelevskyi, L. V. Pourovskii, S. Jiang, K. Kato, C. Yu, Y. Cao, Q. Li, X. Kuang, X. Xing, The structure of terbium in the ferromagnetic state. *J. Am. Chem. Soc.* **145**, 17856–17862 (2023).

18. P. S. Peijzel, A. Meijerink, R. T. Wegh, M. F. Reid, G. W. Burdick, A complete energy level diagram for all trivalent lanthanide ions. *J. Solid State Chem.* **178**, 448–453 (2005).

19. S. Wienholdt, D. Hinzke, K. Carva, P. M. Oppeneer, U. Nowak, Orbital-resolved spin model for thermal magnetization switching in rare-earth-based ferrimagnets. *Phys. Rev. B.* **88**, 020406 (2013).

20. T. A. Ostler, R. F. L. Evans, R. W. Chantrell, U. Atxitia, O. Chubykalo-Fesenko, I. Radu, R. Abrudan, F. Radu, A. Tsukamoto, A. Itoh, A. Kirilyuk, T. Rasing, A. V. Kimel, Crystallographically amorphous ferrimagnetic alloys: Comparing a localized atomistic spin model with experiments. *Phys. Rev. B* **84**, 024407 (2011).

21. U. Atxitia, P. Nieves, O. Chubykalo-Fesenko, Landau-Lifshitz-Bloch equation for ferrimagnetic materials. *Phys. Rev. B* **86**, 104414 (2012).

22. U. Atxitia, T. A. Ostler, Ultrafast double magnetization switching in GdFeCo with two picosecond-delayed femtosecond pump pulses. *Appl. Phys. Lett.* **113**, 062402 (2018).

23. M. Beens, M. L. M. Lalieu, A. J. M. Deenen, R. A. Duine, B. Koopmans, Comparing all-optical switching in synthetic-ferrimagnetic multilayers and alloys. *Phys. Rev. B* **100**, 220409(R) (2019).

24. A. J. Schellekens, B. Koopmans, Microscopic model for ultrafast magnetization dynamics of multisublattice magnets. *Phys. Rev. B* **87**, 020407(R) (2013).

25. J. Stöhr, *NEXAFS Spectroscopy* (Springer Berlin, 2013).

26. L. J. P. Ament, M. van Veenendaal, T. P. Devereaux, J. P. Hill, J. van den Brink, Resonant inelastic x-ray scattering studies of elementary excitations. *Rev. Mod. Phys.* **83**, 705–767 (2011).

27. F. de Groot, A. Kotani, *Core Level Spectroscopy of Solids* (CRC Press, 2008).

28. G. van der Laan, E. Arenholz, Z. Hu, A. Bauer, E. Weschke, C. Schüßler-Langeheine, E. Navas, A. Mühlig, G. Kaindl, J. B. Goedkoop, N. B. Brookes, Magnetic circular dichroism in Tb 3d to 4f resonant photoemission. *Phys. Rev. B* **9**, 8835–8843 (1999).

29. J. K. Lang, Y. Baer, P. A. Cox, Study of the 4f and valence band density of states in rare-earth metals. II. Experiment and results. *J. Phys. F Met. Phys.* **11**, 121–138 (1981).

30. S. I. Anisimov, B. L. Kapeliovich, T. L. Perelman, Electron emission from metal surfaces exposed to ultrashort laser pulses. *Sov. Phys.-JETP* **39**, 375–377 (1974).

31. U. Bovensiepen, Coherent and incoherent excitations of the Gd (0001) surface on ultrafast timescales. *J. Phys.: Condens. Matter.* **19**, 083201 (2007).

32. R. Ahuja, S. Auluck, B. Johansson, M. S. S. Brooks, Electronic structure, magnetism, and Fermi surfaces of Gd and Tb. *Phys. Rev. B* **50**, 5147–5154 (1994).

33. J. J. Rhyne, A. E. Clark, Magnetic Anisotropy of Terbium and Dysprosium. *J. App. Phys.* **38**, 1379–1380 (1967).

34. G. Fitzky, M. Nakajima, Y. Koike, A. Leitenstorfer, T. Kurihara, Ultrafast control of magnetic anisotropy by resonant excitation of 4f electrons and phonons in $Sm_{0.7}Er_{0.3}FeO_3$. *Phys. Rev. Lett.* **127**, 107401 (2021).

35. S. Schlauderer, C. Lange, S. Baierl, T. Ebnet, C. P. Schmid, D. C. Valovcin, A. K. Zvezdin, A. V. Kimel, R. V. Mikhaylovskiy, R. Huber, Temporal and spectral fingerprints of ultrafast all-coherent spin switching. *Nature* **569**, 383–387 (2019).

36. S. Baierl, M. Hohenleutner, T. Kampfrath, A. K. Zvezdin, A. V. Kimel, R. Huber, R. V. Mikhaylovskiy, Nonlinear spin control by terahertz-driven anisotropy fields. *Nat. Photonics* **10**, 715–718 (2016).

37. R. V. Mikhaylovskiy, T. J. Huisman, A. I. Popov, A. K. Zvezdin, T. Rasing, R. V. Pisarev, A. V. Kimel, Terahertz magnetization dynamics induced by femtosecond resonant pumping of Dy^{3+} subsystem in the multisublattice antiferromagnet DyFeO$_3$. *Phys. Rev. B* **92**, 094437 (2015).

38. A. V. Kimel, A. Kirilyuk, A. Tsvetkov, R. V. Pisarev, T. Rasing, Laser-induced ultrafast spin reorientation in the antiferromagnet TmFeO3. *Nature* **429**, 850–853 (2004).

39. N. Koshizuka, K. Hayashi, Raman Scattering from Magnon Excitations in RFeO₃. *J. Physical Soc. Japan* **57**, 4418–4428 (1988).

40. L. Avilés-Félix, A. Olivier, G. Li, C. S. Davies, L. Álvaro-Gómez, M. Rubio-Roy, S. Auffret, A. Kirilyuk, A. V. Kimel, T. Rasing, L. D. Buda-Prejbeanu, R. C. Sousa, B. Dieny, I. L. Prejbeanu, Single-shot all-optical switching of magnetization in Tb/Co multilayer-based electrodes. *Sci. Rep.* **10**, 5211 (2020).

41. K. Mishra, R. M. Rowan-Robinson, A. Ciuciulkaite, C. S. Davies, A. Dmitriev, V. Kapaklis, A. V. Kimel, A. Kirilyuk, Ultrafast demagnetization control in magnetophotonic surface crystals. *Nano Lett.* **22**, 9773–9780 (2022).

42. K. Mishra, T. G. H. Blank, C. S. Davies, L. Avilés-Félix, D. Salomoni, L. D. Buda-Prejbeanu, R. C. Sousa, I. L. Prejbeanu, B. Koopmans, T. Rasing, A. V. Kimel, A. Kirilyuk, Dynamics of all-optical single-shot switching of magnetization in Tb/Co multilayers. *Phys. Rev. Res.* **5**, 023163 (2023).

43. T. Tschentscher, C. Bressler, J. Grünert, A. Madsen, A. P. Mancuso, M. Meyer, A. Scherz, H. Sinn, U. Zastrau, Photon beam transport and scientific instruments at the European XFEL. *Appl. Sci.* **7**, 592 (2017).

44. S. Dziarzhytski, M. Biednov, B. Dicke, A. Wang, P. S. Miedema, R. Y. Engel, J. O. Schunck, H. Redlin, H. Weigelt, F. Siewert, C. Behrens, M. Sinha, A. Schulte, B. Grimm-Lebsanft, S. G. Chiuzbăian, W. Wurth, M. Beye, M. Rübhausen, G. Brenner, The TRIXS end-station for femtosecond time-resolved resonant inelastic x-ray scattering experiments at the soft x-ray free-electron laser FLASH. *Struc. Dyn.* **7**, 054301 (2020).

45. M. Seidel, F. Pressacco, O. Akcaalan, T. Binhammer, J. Darvill, N. Ekanayake, M. Frede, U. Grosse-Wortmann, M. Heber, C. M. Heyl, D. Kutnyakhov, C. Li, C. Mohr, J. Müller, O. Puncken, H. Redlin, N. Schirmel, S. Schulz, A. Swiderski, H. Tavakol, H. Tünnermann, C. Vidoli, L. Wenthaus, N. Wind, L. Winkelmann, B. Manschwetus, I. Hartl, Ultrafast MHz-rate burst-mode pump–probe laser for the FLASH FEL facility based on nonlinear compression of ps-level pulses from an Yb-amplifier chain. *Laser Photonics Rev.* **16**, 2100268 (2022).

46. T. Kachel, F. Eggenstein, R. Follath, A soft X-ray plane-grating monochromator optimized for elliptical dipole radiation from modern sources. *J. Synchrotron Radiat.* **22**, 1301–1305 (2015).

47. M. W. Haverkort, M. Zwierzycki, O. K. Andersen, Multiplet ligand-field theory using Wannier orbitals. *Phys. Rev. B* **85**, 165113 (2012).

48. M. W. Haverkort, G. Sangiovanni, P. Hansmann, A. Toschi, Y. Lu, S. Macke, Bands, resonances, edge singularities and excitons in core level spectroscopy investigated within the dynamical mean-field theory. *EPL* **108**, 57004 (2014).

49. M. W. Haverkort, Quantyfor core level spectroscopy - excitons, resonances and band excitations in time and frequency domain. *J. Phys. Conf. Ser.* **712**, 012001 (2016).

50. F. de Groot, Multiplet effects in X-ray spectroscopy. *Coord. Chem. Rev.* **249**, 31–63 (2005).

51. B. T. Thole, R. D. Cowan, G. A. Sawatzky, J. Fink, J. C. Fuggle, New probe for the ground-state electronic structure of narrow-band and impurity systems. *Phys. Rev. B* **31**, 6856–6858 (1985).

52. R. D. Cowan, *The Theory of Atomic Structure and Spectra* (University of California Press, 1981).

53. J. K. Dewhurst, S. Sharma, The Elk Code (2023); http://elk.sourceforge.net/.

54. P. Blaha, K. Schwarz, G. K.H. Madsen, D. Kvasnicka, J. Luitz, R. Laskowski, F. Tran, L. D. Marks, WIEN2k: An Augmented Plane Wave + Local Orbitals Program for Calculating Crystal Properties (Techn. Universität Wien, 2018).

55. V. I. Anisimov, J. Zaanen, O. K. Andersen, Band theory and Mott insulators: HubbardUinstead of *Stonerl. Phys. Rev. B* **44**, 943–954 (1991).

56. S. Buck, M. Fähnle, Rare-earth magnetic anisotropy: Is the crystal field theory valid? *J. Magn. Magn. Mater.* **166**, 297–302 (1997).

57. M. Richter, "Density functional theory applied to 4f and 5f elements and metallic compounds" in *Handbook of Magnetic Materials*, K. H. J. Buschow, Ed. (Elsevier, 2001), vol. 13, chap. 2, pp. 87–228.

58. T. Hamada, M. Okamoto, First principles calculations of magneto-crystalline anisotropy of rare-earth magnets. *J. Phys. Commun.* **5**, 015013 (2021).

59. M. I. Kaganov, I. M. Lifshitz, L. V. Tanatarov, Relaxation between electrons and crystalline lattice. *JETP* **4**, 173–178 (1957).

60. J. Chen, D. Tzou, J. Beraun, A semiclassical two-temperature model for ultrafast laser heating. *Int. J. Heat Mass Transf.* **49**, 307–316 (2006).

61. R. W. Hill, J. Cosier, D. A. Hukin, P. Wells, P. C. Lanchester, The specific heat of terbium below 4 K. *Phys. Lett. A* **49**, 101–102 (1974).

62. A. Einstein, Die Plancksche Theorie der Strahlung und die Theorie der spezifischen Wärme. *Ann. Phys.* **327**, 180–190 (1907).

63. B. Hüttner, Thermodynamics and transport properties in the transient regime. *J. Phys. Condens. Matter.* **11**, 6757–6777 (1999).

64. J. H. Weaver, C. Krafka, D. W. Lynch, E. E. Koch, *Physik Daten- Optical Properties of metals* (Fachinformationszentrum Karlsruhe, 1981), 20, 1124_1.

65. L. David, Windt, IMD — Software for modeling the optical properties of multilayer films. *Comput. Phys.* **12**, 360–370 (1998).

66. A. Melnikov, H. Prima-Garcia, M. Lisowski, T. Gießel, R. Weber, R. Schmidt, C. Gahl, N. M. Bulgakova, U. Bovensiepen, M. Weinelt, Nonequilibrium magnetization dynamics of gadolinium studied by magnetic linear dichroism in time-resolved 4f core-level photoemission. *Phys. Rev. Lett.* **100**, 107202 (2008).

67. B. T. Thole, G. van der Laan, Branching ratio in x-ray absorption spectroscopy. *Phys. Rev. B* **38**, 3158–3171 (1988).

68. J. Kołaczkiewicz, E. Bauer, The adsorption of Eu, Gd and Tb on the W(110) surface. *Surf. Sci.* **175**, 487–507 (1986).

69. B. Frietsch, R. Carley, K. Döbrich, C. Gahl, M. Teichmann, O. Schwarzkopf, P. Wernet, M. Weinelt, A high-order harmonic generation apparatus for time- and angle-resolved photoelectron spectroscopy. *Rev. Sci. Instrum.* **84**, 075106 (2013).